RESEARCH ARTICLE

Signal decay due to susceptibility-induced intravoxel dephasing on multiple air-filled cylinders: MRI simulations and experiments

**François De Guio · Hugues Benoit-Cattin ·
Armel Davenel**

Abstract

Objective Characterization of magnetic susceptibility artefacts with assessment of the gradient-echo signal decay function of echo time, pixel size, and object geometry in the case of air-filled cylinders embedded in water.

Materials and methods Experiments were performed with a 0.2 T magnet on a network of small interacting air-filled cylinders along with Magnetic resonance imaging (MRI) simulations integrating intravoxel dephasing. Signal decay over echo time was assessed at different pixel sizes on real and simulated images. The effects of radius, distance between cylinders and main magnetic field were studied using simulation.

Results Signal loss was greater as echo time or pixel size increased. Voxel signal decay was not exponential but was weighted by sinus cardinalis functions integrating echo time, pixel size and field inhomogeneities which depended on main magnetic field strength and geometric configuration of the object. Simulation was able to model signal decay, even for a complex object constituted of several cylinders. The specific experimental signal modulation we observed was thus reproduced and explained by simulation.

Conclusion The quantitative signal decay approach at 0.2 T can be used in characterization studies in the case of locally regular air/water interfaces as the signal depends on object size relative to pixel size and is relevant to the geometric configuration. Moreover, the good concordance between simulation and experiments should lead to further studies of magnetic susceptibility effects with other objects such as networks of spheres. MRI simulation is thus a potential tool for molecular and porous media imaging.

Introduction

Porous media are ubiquitous in modern life. Heterogeneities and air inclusions can be found in natural materials (wood, rocks), manmade materials (concretes, food products) and in biological tissues such as lungs and bones. Characterization of the pore structure, including pore size, connectivity and spatial heterogeneity, is important in determining the functions of materials [1,2].

Magnetic resonance imaging (MRI) is a promising non-invasive tool because it provides anatomical and functional information as well as high contrast imaging. However, this technique assumes a perfectly homogeneous field B_0. Variations in magnetic susceptibility between different regions result in field inhomogeneities. Field disturbance is responsible for geometric and intensity distortions in spin-echo (SE) imaging. Misregistration of MRI signal results in focusing of the signal intensity, which produces bright and dark regions in the image [3]. Magnetic susceptibility interfaces also result in additional signal loss in gradient-echo (GE) MR images. This is a result of the MRI signal dephasing within the voxels that are sensitive to the inhomogeneous field around the object, i.e. intravoxel dephasing. Signal loss overshadows geometrical distortions in GE imaging of subvoxel objects [4]. As we used a 0.2 T magnetic field in this

F. De Guio (✉) · A. Davenel
Cemagref, Food Process Engineering Research Unit, CS 64426,
17 avenue de Cucillé, 35 044 Rennes, France
e-mail: francois.de-guio@cemagref.fr

H. Benoit-Cattin
CREATIS, UMR CNRS 5520, Inserm U630,
Université Claude Bernard Lyon 1, INSA Lyon,
Bât. Blaise Pascal, 69 621 Villeurbanne, France

study, geometrical distortions were weak (shift in the image plane was less than 0.1 mm). We were therefore particularly interested in the signal loss phenomenon.

As opposed to some research groups that are trying to correct susceptibility artefacts [5,6], the aim of this study was to characterize them and to use air as a natural marker, a potential contrast agent. Air has the advantage of being present inside many biological or food products and thus could be a signature of the medium. In fact, characterization of these susceptibility artefacts may be of great importance in various types of study. Magnetic susceptibility effects can be used to identify particles in industrial systems [7] or characterize changes in magnetic properties of alloys under thermomechanical stress [8]. In MR angiography the difference in magnetic susceptibility between deoxygenated and oxygenated hemoglobin is used for artery and vein separation [9]. In molecular imaging, injection of paramagnetic markers permits passive tracking [4,10], in the in vivo MR imaging of stem cells [11,12] and qualitative and quantitative assessment of holmium-loaded microspheres [13]. Superparamagnetic iron-oxide (SPIO) nanoparticles have recently been exploited as contrast agents for non-invasive cell tracking, quantification of tissue perfusion and target-specific imaging, and for the detection of gene expression [11,14–21]. Magnetically labeled cells create intense magnetic field distortions within and around the cells, leading to enhanced signal dephasing in GE sequences. In fact, similar causes occur in food products but intensities are much lower due to the weaker magnetic susceptibility differences [22]. The potential application of gas microbubbles as a susceptibility contrast agent for MRI has been demonstrated [23].

Simulation tools have been recognized as effective and important in the field of MRI. They help to understand the complex MR phenomena and they can be used to investigate the causes and effects of artefacts, and for the optimization of MR sequences and validation of image analysis methods [24–28]. While Yoder et al. [26] included field inhomogeneities due to magnetic susceptibility in their simulator; no quantitative comparison has been done with a long echo time exploration and various parameters.

We considered in this study the scale of the field inhomogeneities as summed up in [6]. Microscopic field inhomogeneities are responsible for irreversible signal decay ($R_2 = 1/T_2$), and mesoscopic field inhomogeneities contribute to $R_2^{\#}$, the reversible portion of R_2^* ($R_2^* = R_2 + R_2^{\#} = 1/T_2^*$). Thus, macroscopic field inhomogeneities such as those created by air/water interfaces are not present in T_2^* definition.

Signal decay mechanisms are becoming more significant in data evaluation since susceptibility effects are greater at longer echo times [29]. In fMRI, Sedlacik et al. [30] showed that for certain vessel orientations a significant gradient echo signal recovery occurs at late echo time. Signal decays for a single cylindrical vessel were investigated in simulations and in vivo measurements. Cheng et al. [29] described the complex signal decay for a spherical voxel and found that taken as a whole, the signal may appear multi-exponential. Seppenwoolde et al. [31] simulated signal decay from spectral analysis of induced magnetic field inhomogeneities in the case of cubic voxels. However, these previous studies considered one small object inside one single voxel.

We focused in this study on the signal decay in the static dephasing regime at different pixel sizes in the case of air/water interfaces in 2D GE imaging. Signal behaviors were assessed with both experiments with a 0.2 T magnet and MRI simulation. It is important to underline that we quantitatively assessed signal decay function of echo time along several voxels which undergo spatially dependent field inhomogeneities, making signal analysis closer to reality.

The cylinder model, which is easily applicable to experiments, was used in order to validate our intravoxel modeling. Cylinders were oriented perpendicularly to the main magnetic field as susceptibility artefacts are maximal in this direction [32]. We assessed and explained the signal in the case of an array of small interacting cylinders, studying the impact of pixel size, distance between cylinders and main magnetic field.

Materials and methods

We present in this section both the experimental and simulation parts, two parallel approaches to assess signal loss in the case of a network of cylinders. The main process represented in Fig. 1 was followed from object definition to signal decay computation. Multiple cylinders were chosen because the simulation counterpart can easily be computed, experimental preparation of the object was controlled and such interactions are interesting for characterization purpose in porous media.

Experimental data

MRI device and parameters

A 0.2 T electromagnet scanner in open configuration (Magnetom Open, Siemens, Erlangen, Germany) equipped with a head coil was used to image the objects. For the GE sequences, slice thickness (ST), bandwidth (BW), field of view (FOV) and repetition time (TR) values were set as follows: ST = 5 mm, BW = 156 Hz/pixel, FOV = 256 × 256 mm^2, TR = 1,000 ms. The pixel size was modified by changing the matrix size.

Fig. 1 Overview of the dual approach used for each object to compare experimental and simulated signal decay. In simulation, field inhomogeneities were first computed using a large number of object pixels (pix_{obj}). MR images were then simulated, choosing the number of image pixels (pix_{ima}) to match the real pixel size
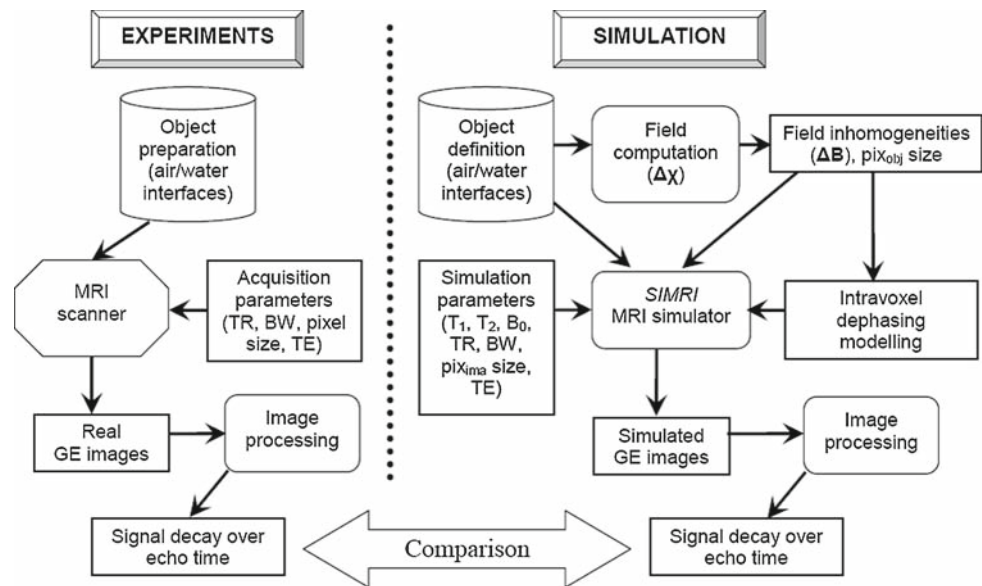
Object preparation

The aim was to observe the signal in the situation of an array of small air-filled cylinders oriented perpendicularly to the main magnetic field.

To achieve this configuration, we perforated a plain sheet of polyurethane foam ($80 \times 80 \times 10$ mm) with 2.25 mm diameter cylindrical holes, spaced at a center to center distance (ccd) of 3 mm. The foam was then soaked with a doped solution (3.2 mM/l $NiSO_4$, 5 g/l $NaCl$; $T_1 = 386$ ms, $T_2 = 386$ ms), drained and imaged in the scanner using a GE sequence with three pixel sizes (0.5, 1 and 2 mm) for TE varying from 8 to 41 ms. An example of an experimental image is depicted in Fig. 2.

Simulated data

Simulation code

The simulation process comprised object definition, computation of its corresponding magnetic field inhomogeneities and simulation of one MRI experiment as illustrated in Fig. 1. We used the SIMRI MRI simulator as described by Benoit-Cattin et al. [25]. Initially, a 3D virtual object was defined, representing a discrete description of a real object spin system. Its size, defined in object pixels (pix_{obj}), was much larger than the simulated image, defined in image pixels (pix_{ima}) to ensure precision in field computation. Each object voxel contained a set of physical values necessary to compute the local spin magnetization vector with the Bloch equation (i.e. proton density, spin-lattice relaxation time T_1 and spin–spin relaxation time T_2). Local main field inhomogeneity
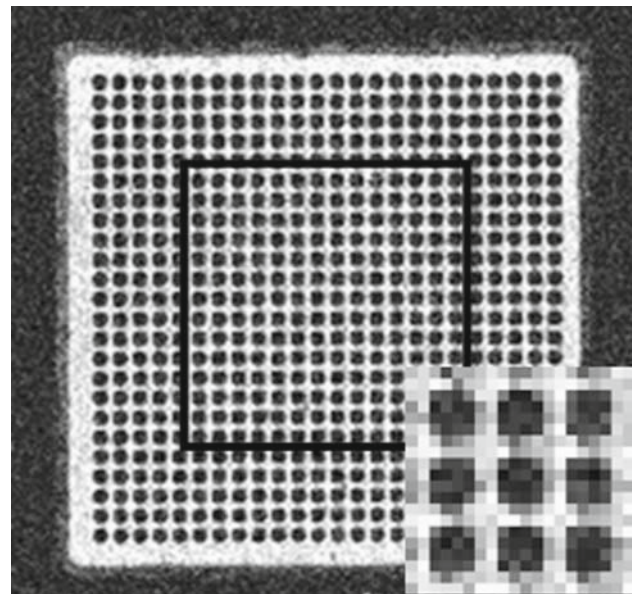

Fig. 2 Experimental GE image of a network of small air-filled cylinders with square ROI. $\varnothing = 2.25$ mm, ccd $= 3$ mm, pixel $= 0.5$ mm, TE $= 8$ ms. Zoom of the image in the *lower right corner* shows the appearance of cylinders with low resolution

ΔB was defined for each virtual object voxel. Constant inhomogeneity within a voxel was assumed.

Object-specific field inhomogeneities were computed before the MRI simulation using a boundary integral method [33] in which the integral was set over the surfaces between the media of different magnetic susceptibilities. The computational procedure consisted of approximating these surfaces with triangular mesh elements and using analytical expressions to compute the integral over each triangle. This method is specifically dedicated to complex objects. In the case of

cylinders, we can also use analytical equations describing field inhomogeneities in space created by one cylinder [3]. As the magnetic field is additive, we added together each cylinder's inhomogeneities to obtain the final field map.

For one simulated MRI experiment, the object is placed in the static field and is excited by electromagnetic events of two types, i.e. RF pulses and magnetic field gradients. The excitation step is followed by the acquisition of the object magnetization state stored as a complex signal in the k-space. The magnetization computation kernel is based on a discrete time solution of the 3D Bloch equation giving the time evolution of the spin magnetization vector. Integrating the field inhomogeneities, SIMRI is able to create the susceptibility effects, i.e. signal loss and geometrical and intensity distortions along the direction of the readout gradient. The susceptibility effects depend on the sequence used, the main field value, the receiver BW and the echo time. For this study, the SIMRI kernel was modified in order to integrate intravoxel dephasing nearly as in [26]. The length of the magnetization vector is affected by the dephasing occurring across a voxel (Eqs. 1, 2). Assuming a linear change across the voxel with a gradient, the modification of the magnetization amplitude in the transverse plane due to magnetic susceptibility effects can be written as follows:

$$M_{xy,\text{dephas}}(t) = M_{xy}(t) \left| \frac{1}{l_x l_y l_z} \int_{-lz/2}^{lz/2} \int_{-ly/2}^{ly/2} \int_{-lx/2}^{lx/2} \times e^{i\gamma t(g_x x + g_y y + g_z z)} \mathrm{d}x \mathrm{d}y \mathrm{d}z \right|$$

$$M_{xy,\text{dephas}}(t) = M_{xy}(t) \left| \sin c(\gamma t g_x l_x/2) \sin c(\gamma t g_y l_y/2) \right. \\ \left. \times \ \sin c(\gamma t g_z l_z/2) \right| \tag{1}$$

with

$$g_i = \frac{1}{2} \frac{(\Delta B_{ip} - \Delta B_{in})}{l_i} \tag{2}$$

where $M_{xy}(t)$ is the magnitude of the magnetization in the xy-plane and $M_{xy,\text{dephas}}(t)$ the magnitude of the magnetization which takes into account the intravoxel dephasing. $\sin c$ is the sinus cardinalis function; l_x, l_y, l_z are the dimensions of the virtual object voxel; γ is the gyromagnetic ratio, ΔB_{ij} is the value of ΔB at the positive neighbor, $j = p$, or the negative neighbor, $j = n$ along the i axis.

Object definition

Before considering a complex object such as a network of cylinders, we validated the intravoxel modeling with a single well-resolved air-filled cylinder. A quantitative study of the signal decay function of echo time at different pixel sizes on

simulated and experimental images was conducted (reported in Appendix A).

In simulation, working with a too large number of cylinders was time-consuming. We therefore defined a 5×5 network of infinite cylinders to study the signal around the central cylinder. Several simulations showed that a 3×3 network was not sufficient and a 7×7 network did not modify the signal found around the central cylinder with the 5×5 configuration. Our virtual cylinders were defined as having a magnetic susceptibility difference $\Delta \chi (\Delta \chi = 9.05\,\text{ppm}$ for air/water interface) between interior and exterior of the cylinders, a 9 pix_{obj} radius and a 24 pix_{obj} ccd inside a 256^2 slice to ensure a precise map of field inhomogeneities (Fig. 3). For a 64^2 simulated image, the radius of each cylinder was 2.25 pix_{ima} and thus equivalent to the experimental situation with the pixel size of 0.5 mm. The situations corresponding to pixel size of 1 and 2 mm were matched with 32^2 and 16^2 simulated images. TE varied from 8 to 44 ms with steps of 2 ms. An example of a simulated image is shown in Fig. 4.

Image processing

Once we had obtained the images (simulated and experimental), it was necessary to define the appropriate measurement, i.e. to study the evolution of the MR signal in relation to echo time. ROIs were thus defined on the experimental and simulated images.
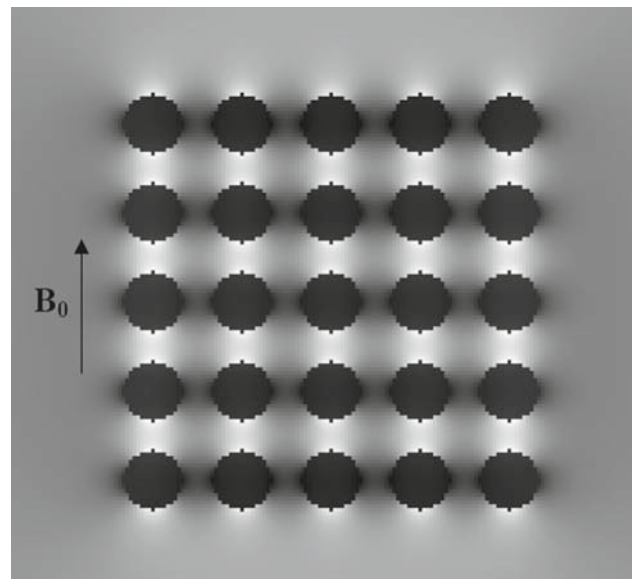

Fig. 3 Field inhomogeneities induced by an object constituted of 25 parallel air-filled cylinders ($r = 9$ pix_{obj}, $ccd = 24$ pix_{obj} in a 256^2 slice) embedded in water. Due to the additive property of the magnetic field, maximum and minimum values were found between two cylinders in columns and rows, respectively
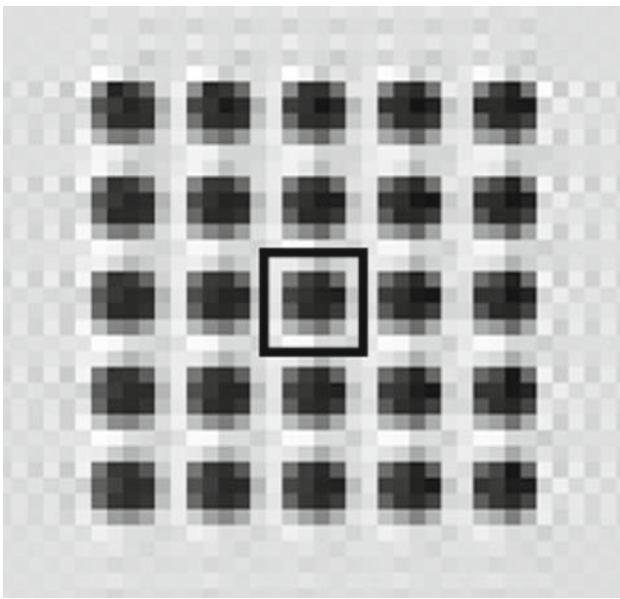
Fig. 4 Non-filtered simulated GE image of a network of air-filled cylinders with square ROI, $\text{pix}_{\text{ima}} = 0.5$ mm, TE = 8 ms. Each cylinder contributed to the intravoxel dephasing and associated signal loss occurring in the ROI

As the object had a homogeneous structure for the experimental network of cylinders, we wanted to characterize the medium. A square enclosing several cylinders (see Fig. 2) was therefore defined. It can be seen that this latter ROI is the combination of small ROIs around one cylinder. We verified that changing the position of the square did not alter the signal emanating from the ROI.

The ROI for the virtual network of cylinders was a square centered on the image and automatically scaled according to the ccd and pixel size (see Fig. 4). The field inhomogeneities induced by the 24 cylinders around the central cylinder contributed to the ROI signal.

On each ROI, the mean gray level (MGL) was computed for simulated and experimental images at each echo time with the different pixel sizes.

Moreover, in order to characterize the signal loss without computing the MGL for each echo time, we defined the normalized signal loss between TE = 8 and 20 ms as:

$$\text{SL}_{8-20} = \frac{\text{GE}_{\text{TE}=8} - \text{GE}_{\text{TE}=20}}{\text{SE}_{\text{TE}=8}} \qquad (3)$$

where $\text{GE}_{\text{TE}} = \tau$ and $\text{S}E_{\text{TE}} = \tau$ are the MGL computed on the scaled centered ROI in the GE and SE images at TE = τ ms. This parameter can be considered as a signal difference due to susceptibility and T_2^* effects normalized by the porosity, as the latter was assessed using SE sequences [34].

Results

Figure 5 summarizes ROI MGL calculated on experimental and simulated images for three different pixel sizes (0.5, 1 and 2 mm). The reference value used for normalization was the ROI MGL at TE = 8 ms and $\text{pix}_{\text{ima}} = 0.5$ mm.

Effects of echo time and pixel size in experiments

As in the case of a single cylinder (Appendix A), signal decayed faster with TE when the pixel was bigger. The 2 mm curve was particularly remarkable as the signal first decreased then increased to a certain local maximum. Thus, the signal decreased to 5% of the reference value for TE = 16 ms and increased to 18% for TE = 27 ms.

Dependence of signal voids on echo time and pixel size was studied to monitor cell migration [4,35], and confirmed these results on signal decay as a function of echo time and pixel size.

The effect of pixel size can be seen as the inverse effect of object size for objects larger than one pixel. Indeed, multiplying the pix_{ima} size by 2 for a given radius is equivalent to keeping the same pix_{ima} size but dividing the radius by 2. In fact, it is the number of pix_{ima} describing the object which it is important to consider.

SIMRI versus experiments

There was a good concordance between simulated and experimental curves. Even the modulation was reproduced in the case of the 2 mm pixel. Slight differences may be explained by considering the experimental objects. The foam cylinders were not very long and were thus not infinite and may not be exactly perpendicular to B_0. Moreover, water could remain in the cylinders during the draining process, thus creating
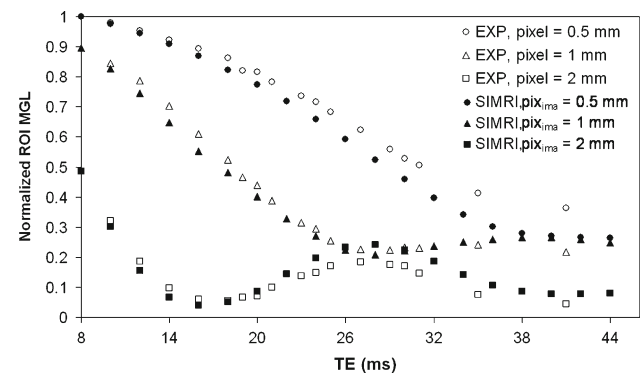

Fig. 5 ROI MGL decay on simulated and experimental images for the network of air-filled cylinders. *MGL decreased more rapidly with TE* when pixel was larger. There was good concordance between simulated and experimental decay even for the remarkable sinc-shaped modulation in the case of a pixel of 2 mm

some undesirable interfaces. The discrete representation of the field maps and object labels, along with the linear approximation of intravoxel dephasing, may also be a reason for the differences observed.

Effect of B_0

We focused in simulation on a given network of air-filled cylinders in water ($r = 1.125$ pix$_{ima}$, ccd $= 3$ pix$_{ma}$). GE images were simulated with another B_0. By choosing $B_0 = 0.8$ T, and comparing with the previous $B_0 = 0.2$ T situation, we showed that an increase in the main magnetic field for a given pixel size induced a faster MGL decrease and a possible modulation which was also observed while increasing pixel size (Fig. 6a).

To demonstrate the impact of B_0 on the MGL, several images were simulated with TE $= 8$ ms and B_0 varying from 0.2 to 3.2 T. Figure 6b shows the effect of B_0 on the ROI MGL characterizing the medium.

The signal first decreased very rapidly with B_0, then oscillated depending on the object's geometric configuration. Applying a higher B_0 to our object resulted in a poor signal and inadequate experimental conditions for observing the
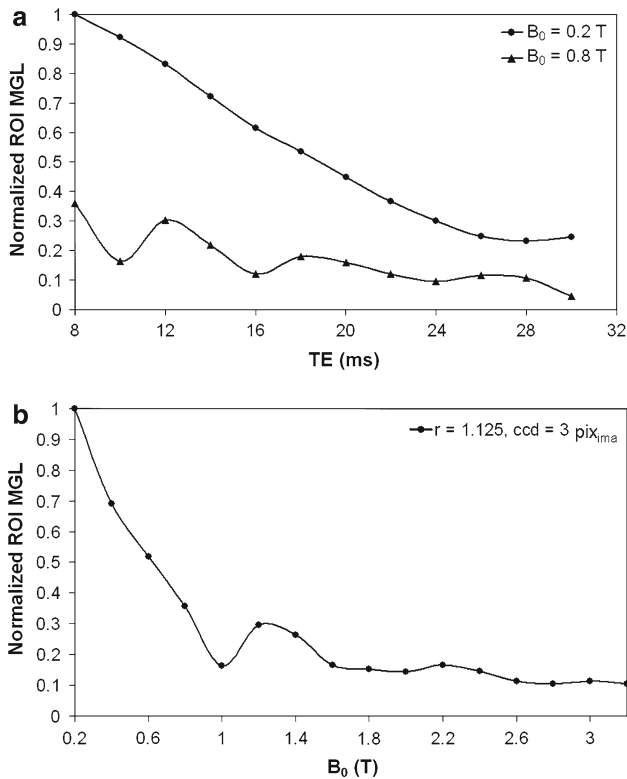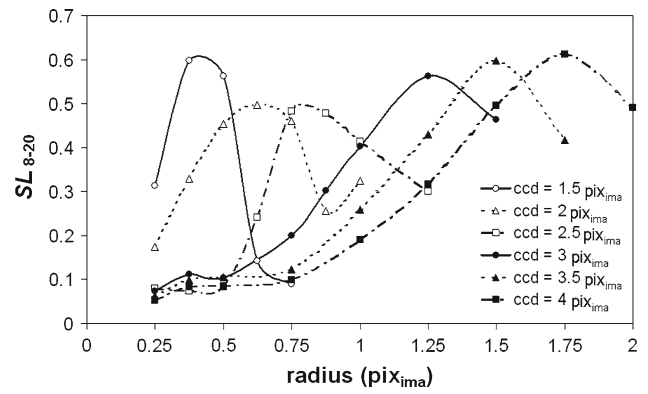

Fig. 7 SL$_{8-20}$ as a function of radius for different ccd. For each ccd, there was a particular radius corresponding to a maximum signal loss

medium. In this study, increasing B_0 resulted in multiplying field inhomogeneities by a constant as the latter were directly proportional to B_0. However, T_1 and T_2 values were not modified according to B_0.

Effects of geometric configuration of multiple cylinders in simulation

In order to analyze the impact of the geometric configuration (radius and ccd) on the MR signal, several dispositions of 5×5 cylinders were simulated with different radii and ccd. We used the SL$_{8-20}$ parameter previously defined in Eq. 3 to characterize the signal loss.

The SL$_{8-20}$ function of the cylinder radius for different ccd is represented in Fig. 7. A hat-shaped curve with a maximum value occurred for each ccd, meaning that signal loss was particularly high for a certain configuration. In fact, we found a linear relation ($R^2 = 0.993$) between ccd and radii for those particular maximum points. At 0.2 T and for air/water susceptibility interfaces, a maximal signal loss was found when ccd $- 1.78 \times$ radius $= 0.86$.

Discussion

Signal decay

For GE sequences, not taking the diffusion effects into account, the voxel signal of volume V decays over time t because of irreversible intravoxel dephasing:

$$S(t)_{voxel} = \frac{1}{V} \int_V p(r) e^{-R_2^*(r)t} e^{-i\gamma \Delta B(r)t} d^3r \qquad (4)$$

where ρ (**r**) is the contribution of the MR signal at position **r**, $\Delta B(\mathbf{r})$ refers to the spatially dependent field inhomogeneity, $R_2^*(\mathbf{r})$ is the effective transverse relaxation rate at position **r** that includes irreversible and reversible

Fig. 6 Effect of B_0 on the ROI MGL for a network of small air-filled cylinders ($r = 1.125$ pix$_{ima}$, ccd $= 3$ pix$_{ima}$). **a** Simulated ROI MGL at $B_0 = 0.2$ and 0.8 T as a function of echo time showing the occurrence of modulation by increasing B_0. **b** Simulated ROI MGL at TE $= 8$ ms as a function of B_0. *MGL* first decreased very rapidly and then oscillated

contributions to signal decay due to microscopic and meso-scopic field inhomogeneities, and γ the gyromagnetic ratio (42.567 MHz T^{-1} for protons). If we consider a constant relaxation rate ($R_2^*(\mathbf{r}) = R_2^* = 1/T_2^*$), a constant MR signal across the voxel ($\rho(\mathbf{r}) = \rho$) of dimensions l_x, l_y, l_z and the expression of the field inhomogeneities along one direction i with a linear gradient ($\Delta B_i = g_i.i$), Eq. 4 can be written as follows:

$$S(t)_{\text{voxel}} = \rho / V.e^{-R_2^* t}. \sin c(\gamma t g_x l_x / 2).$$
$$\times \sin c(\gamma t g_y l_y / 2). \sin c(\gamma t g_z l_z / 2). \qquad (5)$$

Thus, in the absence of background gradients, the MR signal decays exponentially. However, in the presence of field inhomogeneities, the time decay results from the product of exponential $\times$ sin c functions. This explains the signal evolution observed when computing MGL as a function of echo time (Figs. 5, 6a, 9). Defining Θ as the sinus cardinalis argument, then: $\Theta = \gamma.t.g_i.l_i/2$. When Θ increases, i.e. TE, B_0 or pixel size is larger, the sinus period is shorter and thus signal decay is faster. With a high Θ value, a sinus modulation and a local maximum can be observed.

Other research groups have reported a complex signal decay. Seppenwoolde et al. [31] extended Cheng et al.'s [29] studies but used cubic voxels instead of spherical voxels to characterize local deviations in magnetic susceptibility by spectral analysis of their induced magnetic field inhomogeneities. Magnetic resonance spectra and related signal decay curves were simulated for different volume fractions and composition. It first seemed to decay quadratically, then it appeared to decay exponentially and finally slowed its decay or leveled off. However, in these studies, only the signal inside one voxel was taken into account. It is worth noting that the ROI MGL in our study represented the sum of voxel signals with different intravoxel dephasings due to the spatially dependent magnetic inhomogeneities. In fact, the ROI MGL can be seen as an average of different sin c, and thus it was possible to assess the evolution over TE around a susceptibility interface, as in the case of the single cylinder, showing the value of these results to work in 2D.

Apart from experimental parameters (TE, pixel size), one other way of modifying Θ is based on the geometric configuration of the object. Indeed, in the case of multiple cylinders, the further away the cylinders (greater ccd), the less the signal decay rate. Due to the additive property of the magnetic field, magnetic inhomogeneities and thus Θ are greater when cylinders are closer. Signal decay is thus sensitive to the object structure. In the case of a regular medium (same radius and ccd everywhere), study of SL_{8-20} revealed a particular configuration where signal loss was maximal and, given one ccd, there was high sensitivity to the radius. This kind of parameter might permit characterization of a regular medium

when classic image segmentation would fail, i.e. when just a few pixels describe the object.

Pintaske et al. [19] showed that the spatial distribution of magnetic dipoles is an important factor that determines the resonance frequency distribution and hence the MR signal decay. They found the frequency distribution to be non-Lorentzian, which led to non-monoexponential TE-dependent signal decay. However, they did not really study the impact of geometry but expected the geometrical arrangement of subcompartments in which particles clustered to be important.

Still bearing Eq. 5 in mind, we can see the evolution of ROI MGL as a function of the main magnetic field (Fig. 6b) with its oscillations, since $\Delta B_i = g_i.i$ is directly proportional to B_0. In simulation, and given a regular structure, the MR signal can be predicted according to the magnetic field.

Value of a quantitative approach

If B_0 is increased (1.5 T is the routine and enables better resolutions) or $\Delta\chi$ increased (500–1,000 ppm as in contrast agent studies) signal decay is much more rapid. Thus, in order to characterize the signal loss, some research groups have used different approaches. Bos et al. [4] introduced the dephased-volume model which simplifies the effect of a subvoxel susceptibility deviation to a localized suppression of the signal. The artefact is viewed simply as localized removal of the signal from the vicinity of the object. Seppenwoolde et al. [31] characterized local magnetic susceptibility deviations by spectral analysis of their induced magnetic field inhomogeneities.

In a number of studies, T_2^*-weighted GE sequences were used to monitor biodistribution of microspheres. In [13], techniques were investigated for their use in selective internal radiation therapy for liver tumors. To achieve such a goal, the relaxivity of Holmium-loaded microspheres (HoMS) had to be investigated in gel experiments. Generally, the R_2^* is found to be linearly dependent on the concentration, as in [11] with iron oxide-labeled mesenchymal stem cells. However, quantification experiments showed an increasing underestimation for higher doses of HoMS. Qualitative imaging with signal void observation was appropriate for certain studies but involved a critical lack of precision. This was partly due to the spatial distribution and clustering of objects modifying the relaxivity properties [14,36].

However, for a weak susceptibility interface (as for air/water), we can definitely adopt quantitative assessment whereas signal loss depends on echo time, pixel size and geometric configuration.

For porous media like food products signal decay can be considered as a product signature. A 0.2 T magnetic field results in weak induced inhomogeneities and thus longer

echo times. Quantitative assessment is possible, whereas a study of the image void does not reveal much about the object.

It is important to emphasize that low magnetic fields are particularly appropriate for porous media with a particular structure scale and given susceptibility. For much smaller objects, it should be necessary to use a $B_0 = 1.5\,\mathrm{T}$ or higher.

Value of MRI simulation

Study of the signal decay of a single, well resolved cylinder showed the ability of the SIMRI simulator to assess quantitatively the MR signal for a simple susceptibility interface (see Appendix A). This dual approach validated our simulation process instead of a classic comparison between experimental and simulated images. Secondly, a network of regularly spaced small cylinders made it possible to test and validate the SIMRI simulator for a more complex object with a few pixels describing each cylinder. The effects of echo time and pixel size were well assessed in both cases and rendered simulation-only protocols possible. We could thus study the effects of B_0 or geometric configuration on the signal through simulation.

While modeling the vein as an infinitely long cylinder perpendicular to B_0, Xu et al. [37] showed that the apparent phase of a voxel is a function of resolution, vessel size and vessel center in the voxel. MRI simulation can thus be of value in susceptibility weighted imaging and BOLD effect studies.

One application of the virtual array of cylinders could lie in the detection of axon firing in optic nerves in response to visual strobe stimulation. Indeed, the magnetic fields of ionic currents caused by firing of the axons in the optic nerve, which can be represented by a network of parallel cylinders, can cause signal loss due to intravoxel dephasing [38].

Moreover, as the susceptibility difference between bone and fatty marrow is about 3 ppm, field inhomogeneities lead to intravoxel dephasing and signal loss in structural imaging of trabecular bone [39].

There are various possibilities; the requirement is to know the object's geometry with its $\Delta\chi$ spatial distribution and MR parameters (ρ, T_1, T_2). A future study is planned to consider spheres instead of cylinders. The strong dependence of the field inhomogeneities on the signal decay is likely to be of critical importance in optimizing and interpreting systems with magnetic susceptibility interfaces. There are a number of applications in food engineering with air bubbles or quantification of in vivo contrast agents with SPIO and HoMS. For example, given the magnetic susceptibility of particles and geometric dispersion with such a tool, it is possible to predict signal void size on MR images or which particle size to choose to be detectable with a certain resolution. Simulation

could also be helpful when determining protocols for positive contrast MRI of labeled cells [10,14].

In conclusion, MR signal decay due to intravoxel dephasing was studied in the case of a single air-filled cylinder and for a regular medium composed of small cylinders. The behavior was not exponential but weighted by a sinus cardinalis function strongly dependent on pixel size (or object size) and the object's geometry. GE imaging at 0.2 T permits characterization of air/water interfaces. MRI simulation was found to be a powerful tool to deal with specific GE signal loss and decay. Studying different objects such as sphere networks will open up new opportunities to characterize regular media.

Appendix A: Single cylinder quantitative study

Materials and methods

The general framework used for the multiple cylinders object was also followed for the single cylinder case (Fig. 1). The aim was to quantitatively validate the intravoxel modeling included in the simulator SIMRI [25]. This was done by comparing signal decays along a several voxel susceptibility interface for different pixel sizes.

Experimental data

A simple object was required which presented an air/water interface and could be described by a large number of pixels. A 30 mm diameter glass tube with a 1 mm wall and closed with stopper was fixed inside a Plexiglas container. The tube was thus filled with air and surrounded by doped water with the following NMR characteristics: $T_1 = 514\,\mathrm{ms}$, $T_2 = 497\,\mathrm{ms}$. The tube's main axis was perpendicular to the B_0 field. GE images were acquired with the parameters set in "MRI device and parameters". Experiments were run with four pixel sizes (1, 2, 4 and 8 mm) for TE varying from 8 to 160 ms in steps of 4 ms. An example of an experimental image is shown in Fig. 8a.

Simulated data

In this case, we considered an infinite cylinder of radius R containing air ($\chi_{\mathrm{air}} = 0\,\mathrm{ppm}$) and surrounded by water ($\chi_{\mathrm{water}} = -9\,\mathrm{ppm}$). If the main magnetic field B_0 is along the z-axis and cylinder axis along the y-axis, using $\chi \ll 1$ an approximation of the relative field inhomogeneities outside the cylinder [3] is given by:

$$\frac{\Delta B}{B_0}(x, y, z) = \frac{\Delta\chi R^2(x^2 - z^2)}{2(x^2 + z^2)^2}. \tag{6}$$

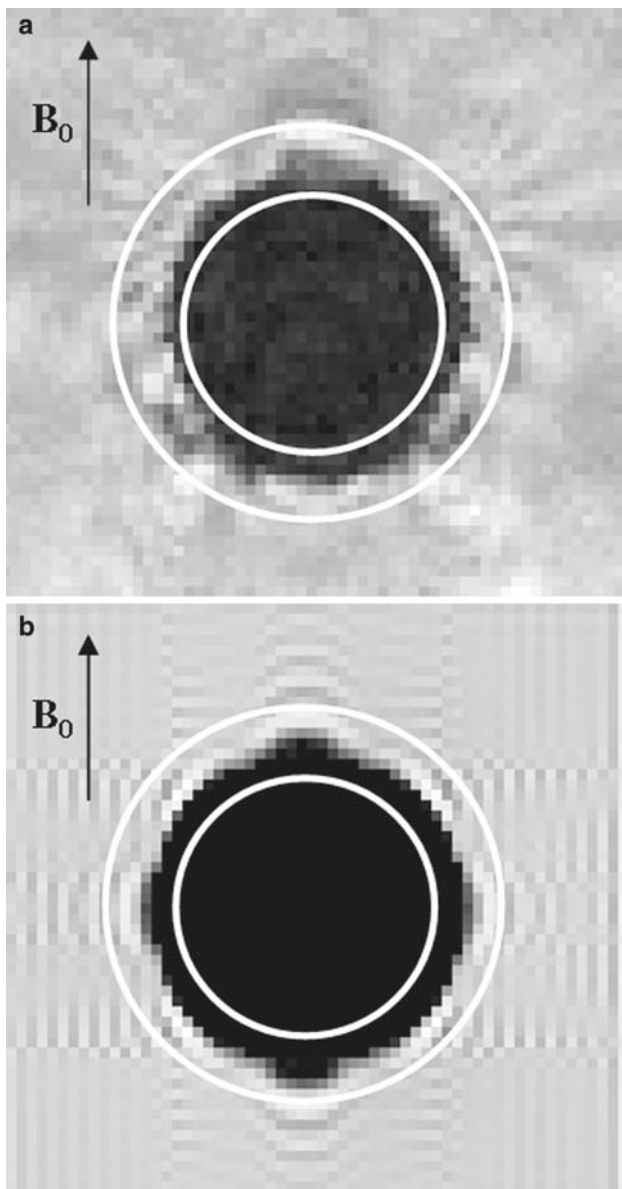In order to match the experimental object, we took into account the 1 mm glass wall separating the air and water

Fig. 8 a Experimental GE image of a single air-filled cylinder with ring-shaped ROI, pixel = 1 mm, TE = 112 ms. Magnetic susceptibility differences induced signal loss near the air/water interface. **b** Non-filtered simulated GE image of a single air-filled cylinder with ring-shaped ROI, pix_{ima} = 1 mm, TE = 112 ms. Signal losses occurred around the interface due to the spatially dependent field inhomogeneities

which represented an undesirable interface. As, like air, glass does not give any signal and has nearly the same magnetic susceptibility as water, the glass wall was considered to be inside our object while dealing with MR simulated signal and to be outside while computing the field inhomogeneities. In numerical terms, the central slice of the virtual cylinder was defined in a 256^2 image with a radius $r = 56$ pix_{obj} for the object labeling ($\rho = 0$ inside, $\rho =$ constant outside) and with $r = 60$ pix_{obj} to compute field inhomogeneities. As we wanted a $pix_{ima} = 1$ mm situation, i.e. $R = 15$ pix_{ima}

to match the single experimental cylinder ($\Phi = 30$ mm), we had to choose a 64^2 pix_{ima} simulated image. Based on similar reasoning for $pix_{ima} = 2$, 4 and 8 mm, we used 32^2, 16^2 and 8^2 pix_{ima} simulated images, respectively. We fixed the same parameters as those used in the MRI experiments: BW = 156 Hz/pixel, TR = 1,000 ms, and we set $B_0 = 0.2$ T, $T_1 = 514$ ms, $T_2 = 497$ ms. Simulations were run with four pix_{ima} sizes (1, 2, 4 and 8 mm) for TE varying from 8 to 160 ms with steps of 4 ms. Figure 8b represents an example of a single cylinder simulated MR image.

Image processing

For the single air-filled cylinder, the aim was to elucidate the signal evolution around the air/water interface. A classic circle around the cylinder does not accurately represent the signal variations due to the large number of low value pixels corresponding to the air. Consequently, a ring-shaped ROI was designed on experimental and simulated images (visible in Fig. 8a, b). The ROI was automatically scaled according to the pixel size.

Results

We gathered the ROI MGL computed on experimental and simulated images in the same plot (Fig. 9) as a function of echo time for pixel size equal to 1, 2, 4 and 8 mm. We also added the signal computed in a reference ROI, i.e. with no object-induced magnetic susceptibility differences, to obtain the T_2^* curve and to compare our data.

Effects of echo time and pixel size in experiments

It can clearly be seen in Fig. 9 that signal loss increased (as MGL decreased) with TE and was greater as pixel size
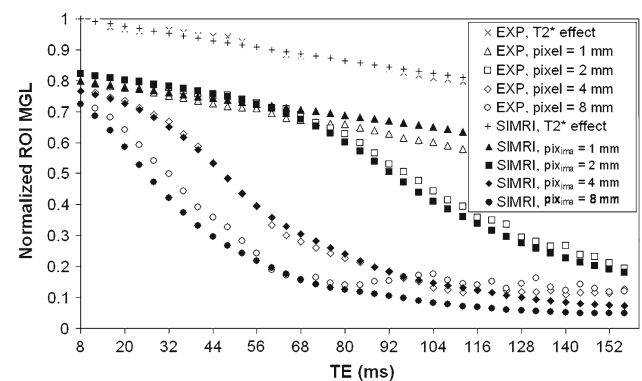

Fig. 9 ROI signal decays on simulated and experimental images for the single air-filled cylinder. *MGL* decayed with *TE* and was more rapid as pixel size increased. The T_2^* effect curve represented the ROI MGL decay in the absence of object-induced field inhomogeneities. Experimental and simulated curves were congruent

increased. We assessed the reference T_2^* curve, i.e. the signal decay mainly due to the T_2 effect and partly due to the inherent mesoscopic field inhomogeneities. For the smallest pixel (1 mm), the experimental ROI MGL decreased slowly with TE in the same way as the T_2^* effect because susceptibility effects seemed to be weak. Indeed, signal loss between 8 and 44 ms was nearly 8% whereas signal loss due to the T_2^* effect was 6%. This small difference can be explained by the glass wall which did not contribute to the MR signal. In the case of the 2 mm pixel, susceptibility effects were clearly visible at long echo times and signal decay was no longer similar to the T_2^* decrease. Note that signal started to be different from the 1 mm curve around 70 ms. Signal losses increased with pixel size. Between 8 and 44 ms, signal loss was 30% for a pixel of 4 mm and 50% for a pixel of 8 mm.

SIMRI versus experiments

The simulated curves were similar to the experimental curves. They were in very good agreement except in the case of a pixel = 8 mm. This can be explained by considering the weak resolution in simulated images which required ROI of a few pixels sensitive to partial volume effects. For TE greater than 80 ms, the experimental curve was affected by noise not present in simulations.

References

1. Song Y-Q (2003) Using internal magnetic fields to obtain pore size distributions of porous media. Concepts Magn Reson Part A Bridg Educ Res 18(2):97–110
2. Chen Q, Marble AE, Colpitts BG, Balcom BJ (2005) The internal magnetic field distribution and single exponential magnetic resonance free induction decay, in rocks. J Magn Reson 175(2):300–308
3. Ludeke KM, Roschmann P, Tischler R (1985) Susceptibility artefacts in NMR imaging. Magn Reson Imaging 3(4):329–343
4. Bos C, Viergever MA, Bakker CJG (2003) On the artifact of a subvoxel susceptibility deviation in spoiled gradient-echo imaging. Magn Reson Med 50(2):400–404
5. Chen NK, Wyrwicz AM (1999) Removal of intravoxel dephasing artifact in gradient-echo images using a field-map based RF refocusing technique. Magn Reson Med 42(4):807–812
6. Fernandez-Seara MA, Wehrli FW (2000) Postprocessing technique to correct for background gradients in image-based R2* measurements. Magn Reson Med 44(3):358–366
7. Robson P, Hall L (2005) Identifying particles in industrial systems using MRI susceptibility artefacts. AIChE J 51(6):1633–1640
8. Peeters JM, van Faassen EEH, Bakker CJG (2006) Magnetic resonance imaging of microstructure transition in stainless steel. Magn Reson Imaging 24(5):663–672
9. Wang Y, Yu Y, Li D, Bae KT, Brown JJ, Lin W, Haacke EM (2000) Artery and vein separation using susceptibility-dependent phase in contrast-enhanced MRA. J Magn Reson Imaging 12(5):661–670
10. Seppenwoolde JH, Viergever MA, Bakker CJG (2003) Passive tracking exploiting local signal conservation: the white marker phenomenon. Magn Reson Med 50(4):784–790
11. Ittrich H, Lange C, Togel F, Zander AR, Dahnke H, Westenfelder C, Adam G, Nolte-Ernsting C (2007) In vivo magnetic resonance imaging of iron oxide-labeled, arterially-injected mesenchymal stem cells in kidneys of rats with acute ischemic kidney injury: Detection and monitoring at 3T. J Magn Reson Imaging 25(6):1179–1191
12. Bos C, Delmas Y, Desmouliere A, Solanilla A, Hauger O, Grosset C, Dubus I, Ivanovic Z, Rosenbaum J, Charbord P, Combe C, Bulte JWM, Moonen CTW, Ripoche J, Grenier N (2004) In vivo MR imaging of intravascularly injected magnetically labeled mesenchymal stem cells in rat kidney and liver. Radiology 233(3):781–789
13. Seppenwoolde JH, Nijsen JFW, Bartels LW, Zielhuis SW, Schip ADV, Bakker CJG (2005) Internal radiation therapy of liver tumors: qualitative and quantitative magnetic resonance imaging of the biodistribution of holmium-loaded microspheres in animal models. Magn Reson Med 53(1):76–84
14. Cunningham CH, Arai T, Yang PC, McConnell MV, Pauly JM, Conolly SM (2005) Positive contrast magnetic resonance imaging of cells labeled with magnetic nanoparticles. Magn Reson Med 53(5):999–1005
15. Yoshikawa T, Mitchell DG, Hirota S, Ohno Y, Oda K, Maeda T, Fujii M, Sugimura K (2006) Gradient- and spin-echo T2-weighted imaging for SPIO-enhanced detection and characterization of focal liver lesions. J Magn Reson Imaging 23(5):712–719
16. Dunning MD, Kettunen MI, Constant CF, Franklin RJM, Brindle KM (2006) Magnetic resonance imaging of functional Schwann cell transplants labelled with magnetic microspheres. Neuroimage 31(1):172–180
17. Jensen JH, Chandra R (2002) Theory of nonexponential NMR signal decay in liver with iron overload or superparamagnetic iron oxide particles. Magn Reson Med 47(6):1131–1138
18. Corot C, Robert P, Idee JM, Port M (2006) Recent advances in iron oxide nanocrystal technology for medical imaging. Adv Drug Deliv Rev 58(14):1471–1504
19. Pintaske J, Muller-Bierl B, Schick F (2006) Effect of spatial distribution of magnetic dipoles on Lamor frequency distribution and MR signal decay—a numerical approach under static dephasing conditions. Magn Reson Mater Phys 19(1):46–53
20. Oweida AJ, Dunn EA, Karlik SJ, Dekaban GA, Foster PJ (2007) Iron-oxide labeling of hematogenous macrophages in a model of experimental autoimmune encephalomyelitis and the contribution to signal loss in fast imaging employing steady state acquisition (FIESTA) images. J Magn Reson Imaging 26(1):144–151
21. Mowat P, Franconi F, Chapon C, Lemaire L, Dorat J, Hindre F, Benoit JP, Richomme P, Le Jeune JJ (2007) Evaluating SPIO-labelled cell MR efficiency by three-dimensional quantitative T-2* MRI. NMR Biomed 20(1):21–27
22. Bonny J-M, Rouille J, Della Valle G, Devaux M-F, Douliez J-P, Renou J-P (2004) Dynamic magnetic resonance microscopy of flour dough fermentation. Magn Reson Imaging 22(3):395–401
23. Wong KK, Huang I, Kim YR, Tang H, Yang ES, Kwong KK, Wu EX (2004) In vivo study of microbubbles as an MR susceptibility contrast agent. Magn Reson Med 52(3):445–452
24. Bittoun J, Taquin J, Sauzade M (1984) A computer algorithm for the simulation of any nuclear magnetic resonance (NMR) imaging method. Magn Reson Imaging 2(2):113–120
25. Benoit-Cattin H, Collewet G, Belaroussi B, Saint-Jalmes H, Odet C (2005) The SIMRI project: a versatile and interactive MRI simulator. J Magn Reson 173(1):97–115
26. Yoder DA, Zhao Y, Paschal CB, Fitzpatrick JM (2004) MRI simulator with object-specific field map calculations. Magn Reson Imaging 22(3):315–328

27. Jochimsen TH, Schafer A, Bammer R, Moseley ME (2006) Efficient simulation of magnetic resonance imaging with Bloch–Torrey equations using intra-voxel magnetization gradients. J Magn Reson 180(1):29–38

28. Muller-Bierl BM, Graf H, Pereira PL, Schick F (2006) Numerical simulations of intra-voxel dephasing effects and signal voids in gradient echo MR imaging using different sub-grid sizes. Magn Reson Mater Phys 19(2):88–95

29. Cheng YCN, Haacke EM, Yu YJ (2001) An exact form for the magnetic field density of states for a dipole. Magn Reson Imaging 19(7):1017–1023

30. Sedlacik J, Rauscher A, Reichenbach JR (2007) Obtaining blood oxygenation levels from MR signal behavior in the presence of single venous vessels. Magn Reson Med 58(5):1035–1044

31. Seppenwoolde JH, van Zijtveld M, Bakker CJG (2005) Spectral characterization of local magnetic field inhomogeneities. Phys Med Biol 50(2):361–372

32. Guermazi A, Miaux Y, Zaim S, Peterfy CG, White D, Genant HK (2003) Metallic artefacts in MR imaging: effects of main field orientation and strength. Clin Radiol 58(4):322–328

33. Balac S, Benoit-Cattin H, Lamotte T, Odet C (2004) Analytic solution to boundary integral computation of susceptibility induced magnetic field inhomogeneities. Math Comput Model 39 (4–5):437–455

34. Grenier A, Lucas T, Collewet G, Le Bail A (2003) Assessment by MRI of local porosity in dough during proving. Theoretical considerations and experimental validation using a spin-echo sequence. Magn Reson Imaging 21(9):1071–1086

35. Pintaske J, Muller-Bierl B, Schick F (2006) Geometry and extension of signal voids in MR images induced by aggregations of magnetically labelled cells. Phys Med Biol 51(18):4707–4718

36. Tanimoto A, Oshio K, Suematsu M, Pouliquen D, Stark DD (2001) Relaxation effects of clustered particles. J Magn Reson Imaging 14(1):72–77

37. Xu Y, Haacke EM (2006) The role of voxel aspect ratio in determining apparent vascular phase behavior in susceptibility weighted imaging. Magn Reson Imaging 24(2):155–160

38. Chow LS, Cook GG, Whitby E, Paley MNJ (2006) Investigating direct detection of axon firing in the adult human optic nerve using MRI. Neuroimage 30(3):835–846

39. Techawiboonwong A, Song HK, Magland JF, Saha PK, Wehrli FW (2005) Implications of pulse sequence in structural imaging of trabecular bone. J Magn Reson Imaging 22(5):647–655